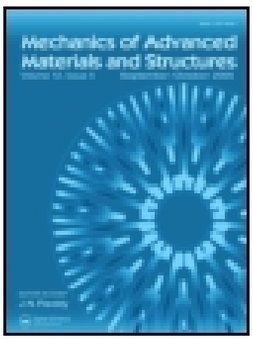

Mechanics of Advanced Materials and Structures

ISSN: 1537-6494 (Print) 1537-6532 (Online) Journal homepage: https://www.tandfonline.com/loi/umcm20

Novel LHC collimator materials: High-energy Hadron beam impact tests and nondestructive postirradiation examination

Giorgia Gobbi, Alessandro Bertarelli, Federico Carra, Jorge Guardia-Valenzuela & Stefano Redaelli

To cite this article: Giorgia Gobbi, Alessandro Bertarelli, Federico Carra, Jorge Guardia-Valenzuela & Stefano Redaelli (2019): Novel LHC collimator materials: High-energy Hadron beam impact tests and nondestructive postirradiation examination, Mechanics of Advanced Materials and Structures, DOI: 10.1080/15376494.2018.1518501

To link to this article: https://doi.org/10.1080/15376494.2018.1518501

Published online: 18 Jan 2019.

MECHANICS OF ADVANCED MATERIALS AND STRUCTURES
https://doi.org/10.1080/15376494.2018.1518501

Novel LHC collimator materials: High-energy Hadron beam impact tests and nondestructive postirradiation examination

Giorgia Gobbi[a], Alessandro Bertarelli[a], Federico Carra[a], Jorge Guardia-Valenzuela[a,b], and Stefano Redaelli[a]

[a]CERN, Geneva, Switzerland; [b]Advanced Microscopy Laboratory (LMA), Institute of Nanoscience of Aragon (INA), University of Zaragoza, Zaragoza, Spain

ABSTRACT

The LHC collimation system must adopt materials with excellent thermal shock resistance, high electrical conductivity, geometrical stability, and radiation hardness. Two novel composites, Molybdenum–Carbide–Graphite and Copper–Diamond, are proposed for the LHC collimation upgrade. A postirradiation examination was performed to assess the status of the composites, tested under intense proton beam impacts at the CERN HiRadMat facility. Metrology measurements, computed tomography, and 3D topography allowed to evaluate the localized spallation induced by the beam. This article provides an overview of the thermophysical characterization of the two composites before irradiation and nondestructive postirradiation results.

ARTICLE HISTORY
Received 28 August 2018
Accepted 28 August 2018

KEYWORDS
Graphite and diamond composites; HL-LHC collimators; Hadron beam impacts; nondestructive tests

1. Introduction

The CERN Large Hadron Collider (LHC) [1] is the largest and most energetic particle accelerator in the world, with two counter rotating proton beams, having a design stored energy of 360 MJ each, circulating in a ring installed in a 27-km long underground tunnel. Superconductive magnets producing an 8.3 T magnetic field, cooled in a bath of superfluid helium, guide the particles over their circular orbit. The two beams are accelerated inside the ring with a radio-frequency system and then brought into collision inside four detectors—ALICE, ATLAS, CMS, and LHCb. The energy stored in the beams will be almost doubled in the next years with the High Luminosity LHC (HL-LHC) upgrade [2], aimed at increasing the machine performances. In such operational conditions, the unavoidable beam losses could compromise the functioning of other components, e.g. magnets. Therefore, the LHC is endowed with a collimation system [3], whose main functions are removing stray particles, which would induce quenches in the superconductive magnets, and shielding the other machine components in case of accidental beam impacts. The complete LHC collimation system comprises about 50 collimators per beam. A scheme of an HL-LHC collimator is showed in Figure 1.

A collimator consists mainly of two movable girders (jaws), contained in an austenitic stainless steel vacuum tank, which are placed at a distance as small as 1 mm from the circulating particle beam axis. The jaw movement along the collimator plane (horizontal in the example of Figure 1) is performed by means of an actuation system based on four stepper motors and leadscrews. There is also a vertical movement of ±10 mm given to the full tank through a 5th axis. Each jaw is made of an absorber, the element actively intercepting the beam particles, clamped on a support in oxide-dispersion-strengthened copper (Glidcop®Al-15), called housing. The total active length of the absorber is up to 1 m, achievable either with a monolithic block of material or by means of adjacent shorter blocks. As will be explained later in this article, since the jaws operate close to the beams, the absorber surface flatness must be extremely small (100 µm over 1 m) to avoid perturbing effects on the traveling protons and to ensure the cleaning efficiency. A cooling circuit, made of CuNi 90-10 alloy and brazed to the housing, permits to limit the temperature reached on the jaws during operation. Notably, the thermal conductance to be achieved by the brazing to ensure an effective cooling performance is 9000 $W \cdot m^{-2} \cdot K^{-1}$. Three plates in Glidcop®Al-15, arranged in a C-shape around the housing, reduce the bending deformation of the structure induced by thermal and mechanical loads. To improve the efficiency of the collimation system, in the LHC there are vertical, horizontal, and skew collimators, named according to the jaw movement with respect to the beam.

The multistage LHC collimation system is based on a well-defined transverse hierarchy, including primary, secondary, and tertiary collimators, with the jaws opened by an increasing transversal distance from the beam, i.e. aperture. Additional collimators are part of this transverse hierarchy for different purposes, like shower absorbers for magnet protection. The main difference among the collimator categories consists in the absorber materials. Normally, for primary and secondary collimators, which operate closer to the beam and are therefore exposed to higher losses, low-density

CONTACT Giorgia Gobbi giorgia.gobbi@cern.ch European Organization for Nuclear Research, Genève, 1211 Switzerland.

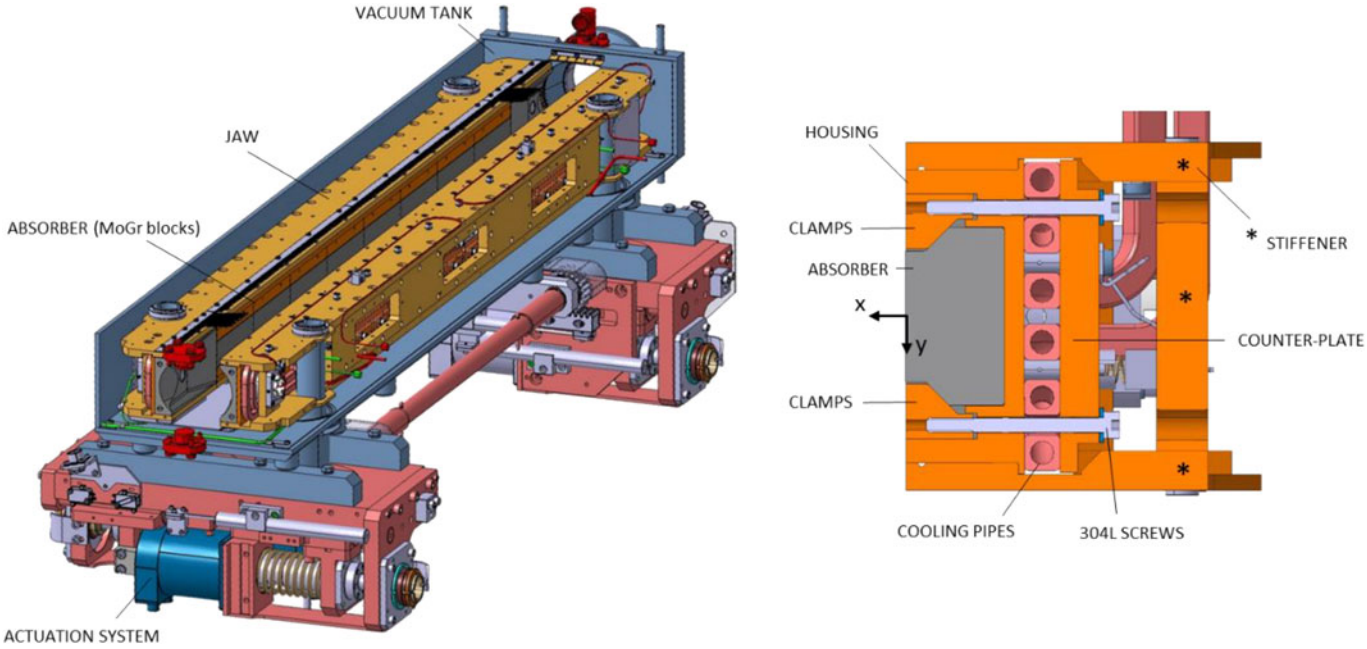

Figure 1. Scheme of a HL-LHC collimator (left) and transverse cross section of the collimator jaw (right).

absorber materials are used. This reduces the energy absorption ensuring higher thermomechanical robustness. On the other hand, for tertiary collimators and shower absorbers, since they are retracted further from the beam axis and in the shadow of primaries and secondaries, denser materials are necessary. They represent the last barrier of protection of delicate components, so robustness is traded for better absorption. Currently, carbon fiber-reinforced carbon (CFC) is adopted for primary and secondary collimators, while the tungsten alloy Inermet®180 is used for the tertiaries. Due to the interaction with intense and energetic particle beams, the absorber materials embarked in collimators must withstand extreme conditions of temperature and stress, in particular under accidental impact cases. This means that collimator materials must satisfy a wide range of requirements that can be quantified in terms of thermomechanical properties [4]. Specifically, thermal conductivity and specific heat must be high to guarantee geometrical stability under slow losses. The melting temperature should be high as well, to allow the material to survive the accidental case conditions. On the other hand, coefficient of thermal expansion and density should be low, to increase the thermal shock resistance and to limit the peak energy deposition, respectively. Moreover, additional requirements include high electrical conductivity, machinability, radiation hardness, and low magnetic susceptibility. No existing material fully satisfies all these conflicting requirements, which will be even more demanding under the HL-LHC upgrade. Therefore, a far-reaching R&D activity was launched at CERN to develop novel materials suitable for collimation applications. The purpose was to combine the properties of graphite or diamond, in particular low density, high thermal conductivity, and low thermal expansion, with those of metals or transition metal-based ceramics, such as high mechanical strength and good electrical conductivity. Among the materials studied in the framework of this R&D activity [5–7], the most promising ones were Molybdenum–Carbide–Graphite (MoGr) and Copper–Diamond (CuCD). Both materials were comprehensively characterized from a thermophysical point of view, in the Mechanical Measurement Laboratory at CERN. Moreover, they were tested under high-energy beam impact in the HiRadMat facility [8] at CERN, to assess their behavior in the real conditions expected in the LHC. These two materials are currently baseline options for HL-LHC collimators [2], in particular MoGr for primaries and secondaries, while CuCD, because of its higher density, for tertiary collimators.

2. Novel collimator materials

In this section, details concerning the two novel materials proposed for the HL-LHC collimators will be presented, together with the results of their thermophysical characterization.

2.1. Molybdenum–Carbide–Graphite

Molybdenum–Carbide–Graphite (Figure 2) was co-developed and patented by CERN and an Italian company, Brevetti Bizz. It is a sintered material obtained starting from powders of graphite, molybdenum, carbon fibers, and/or titanium depending on the grades [9]. In particular, in the grade described in this article and tested in HiRadMat (MG-6530Aa according to the naming conventions defined in [9]), only carbon fibers are added, while titanium is not present. The powder mixture consists of graphite spheroidal flakes with an average diameter of about 30 μm, molybdenum particles with an average size of 5 μm and carbon fibers with a diameter of 10 μm and a length of 250 μm. The percentage in volume of each constituent is reported in

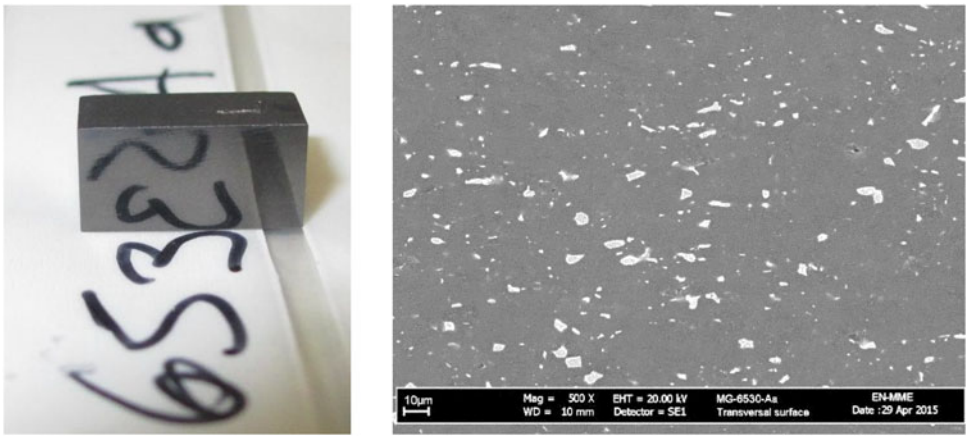

Figure 2. SEM observation of MoGr polished surface perpendicular to the graphite basal planes. Graphite matrix in dark gray and carbide particles in light gray.

Table 1. MoGr (grade MG-6530Aa) composition and production process parameters.

	Volumetric %	
Graphite	90.5	
Molybdenum	4.5	
Carbon fibers	5	
	Sintering cycle	Post-sintering thermal treatment
Temperature (°C)	~2600	~2100
Time (s)	2400	3000
Pressure (MPa)	35	0

Table 2. Thermophysical properties of MoGr and CuCD, parallel (||), and perpendicular (⊢) to graphite basal planes.

	MoGr orientation		
Properties	||	⊢	CuCD
Density ($g \cdot cm^{-3}$)	2.51		5.25
CTE RT-200 °C ($\mu m \cdot m^{-1} \cdot K^{-1}$)	1.7	11.6	6.56
Thermal conductivity ($W \cdot m^{-1} \cdot K^{-1}$)	706	47	338
Thermal diffusivity ($mm^2 \cdot s^{-1}$)	469	31	189
Specific heat ($J \cdot g^{-1} \cdot K^{-1}$)	0.60		0.34
Electrical conductivity ($MS \cdot m^{-1}$)	0.69	–	8.2
Young's modulus (GPa)	76.7	4.7	160
Flexural strength (MPa)	80	11.5	104
Flexural strain to failure ($\mu m \cdot m^{-1}$)	1960	5140	5750

Table 1, together with the parameters of the sintering and postsintering thermal treatment processes.

The powder mixture is compacted at room temperature in a green body, then sintered by means of Spark Plasma Sintering (SPS). This technique implies the use of electric current through the sintered material and mold to generate heat. The material is produced by liquid-phase sintering, at a temperature slightly above the melting temperature of the carbides (2589 °C), formed by Molybdenum–Carbon reaction at high temperature. After sintering, a stress relieving heat treatment at a temperature exceeding 2000 °C for almost 1 h is performed. As a result, the material is orthotropic. It is made of a graphite matrix, whose basal planes are oriented perpendicularly to the direction of the pressing force, with a dispersion of molybdenum carbide particles. Molybdenum carbides improve the bonding between graphite planes, thus reducing the anisotropy of the composite. A summary of the thermophysical properties is reported in Table 2, together with those of CuCD [10].

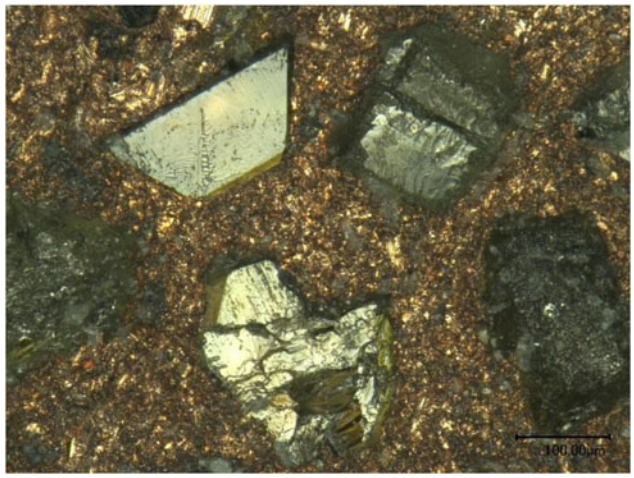

Figure 3. Optical microscope image of copper–diamond surface.

2.2. Copper–Diamond

Copper–Diamond (Figure 3) is a composite material developed by the Austrian company RHP Technology by solid-state sintering with SPS technique [11]. Due to the low chemical affinity between copper and diamond, a third element, boron in this case, is added as binder. During the sintering process, this element promotes the formation of carbides at the copper–diamond interface, improving the material internal bonding. The quantity of diamond must stay below a threshold value to ensure a good compaction of the material. With this purpose, diamond particles with different sizes were used in the powder mixture. In particular, 90% of the total amount has dimensions of about 100 µm and the remaining 10% of around 40 µm. Finished components made of this material are usually produced using a sandwich setup, meaning a metallic copper layer up to 100 µm on the external surfaces, and the copper–diamond composites in the bulk. This softer copper cladding enables dimensional tolerances and surface finishes to be achieved more easily. The initial composition of the material, together with the production process parameters, is reported in Table 3.

3. Materials under beam impact

The collimator materials in operation are impacted by high-energy circulating particles. These particles transfer their

Table 3. CuCD composition and production process parameters.

	Volumetric %	
Diamonds	60	
Copper	39	
Boron	1	
	Sintering cycle	Post-sintering thermal treatment
Temperature (°C)	~1020	~250
Time (s)	1800	1800
Pressure (MPa)	30	0

kinetic energy to the material under the form of thermal energy. In nominal conditions, only the stray particles of the beam are intercepted by the absorbers, thus entailing a steady thermal load on the material. On the other hand, in accidental case scenarios it can happen that the full beam impacts the collimator. In this case, the interaction time is typically very short (few μs), and therefore the dynamic structural response of the absorber is excited. In these conditions, stress and shock waves generate and propagate through the structure.

3.1. Theoretical aspects

Let us consider the case of a thick target, for example a collimator block, impacted by a particle beam. The pulse induces a local temperature and pressure increase inside the material, with a possible phase change. A compressive cylindrical wave is developed, propagating radially with a velocity *U*. The amplitude wave decays while traveling in the surrounding material, as the energy is spread over an increasing volume. When the compressive wave reaches a free surface, it is reflected into a tensile one.

Three main scenarios may occur, as schematically shown in Figure 4. Condition A: in case of impact close to a free surface, the compressive wave turns into a tensile wave after reflection at the free edge and may provoke spallation fracture, if the spall strength of the material is exceeded. Condition B: in case of impact further from the surface or high spall strength material, only plastic deformation arises at the free surface. Condition C: in the particular case of a grazing impact with a phase change induced in the material at the free surface, microspall, and/or microjetting take place. When the liquid surface reflects the pressure wave, the tensile stresses arising cannot be sustained by the material, which is pulverized into minuscule droplets (microspalls). If the surface remains solid but the inner pressure of the liquid or gas volume is high enough to provoke its fracture, a spray of liquid, gas, and solid particles is ejected from the surface (microjetting) [12].

To predict the response of collimator materials in operation, two complementary techniques can be adopted: numerical simulations and experimental tests. These methods should be used in parallel, in particular when extreme conditions of pressure, temperature, and strain are expected.

3.2. Numerical methods

Numerical techniques make use of material models built with the properties derived from laboratory characterization,

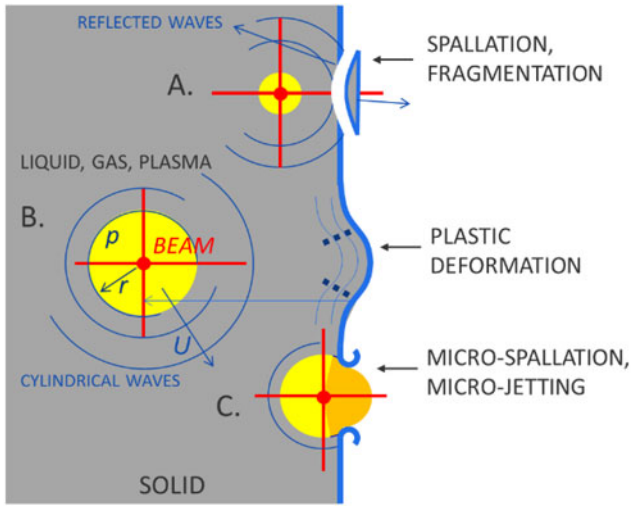

Figure 4. Phenomena occurring in case of beam impact on a thick target.

such as those shown in Table 2. The method consists of a chain of simulations including an energy deposition code, *e.g.* FLUKA [13] or GEANT4 [14], and a finite element (FE) code, e.g. ANSYS [15] and Autodyn [16].

The energy deposition codes, based on a Monte Carlo method, calculates the thermal energy deposited by the particle beam on a target. The code provides the specific energy in GeV/cm^3 calculated at each element of the finite element mesh and normalized to one proton. This needs, then, to be scaled according to the total particle intensity of the beam. When a beam impacts a target, the beam particles interact both with electrons and nuclei of the target material. The beam-nuclei interaction generates secondary particles, called particle shower that may in turn be absorbed by the material. Therefore, the energy deposition is a material-dependent feature. High density and high atomic number materials have high energy stopping power and thus high energy density will be induced during the impact.

The thermal energy maps produced by energy deposition codes are then imported as an input for the dynamic finite element simulations, performed with ANSYS or Autodyn, to evaluate the material thermomechanical response. ANSYS implicit is typically adopted for the cases involving a negligible density change, which can be treated to a good approximation with a simplified, linear equation of state. Autodyn, on the other hand, is an explicit FE code particularly suitable in more extreme scenarios, encompassing a relevant change of temperature, density and pressure. The code is particularly powerful when simulating the shockwave regime, as well as in the cases of material explosion/fragmentation, which can be well treated with the Smoothed-Particle Hydrodynamics (SPH) method. Examples of such simulations are presented in [12].

3.3. Experimental techniques

The experimental testing of materials under beam impact can be performed in facilities such as *High irradiation to Materials* (HiRadMat) at CERN, in which it is possible to irradiate targets with high-intensity proton and ion beam pulses. The facility uses the beam extracted from the CERN

Super Proton Synchrotron, the injector of the LHC that can currently reach, in the case of a proton beam, a maximum stored energy of 2.6 MJ at 440 GeV and a pulse length of 7.2 μs. Different impact scenarios, with variable energy densities, can be explored by changing the beam intensity (i.e. number of particles) and the beam size spot at the target. The density of the impacting beam, in the plane orthogonal to the propagation direction, follows a Gaussian distribution. The parameter σ is its standard deviation and defines the beam transverse size. The HiRadMat allowable σ-range is 0.1–2 mm.

4. HRMT-23 experiment

In 2015, an experiment, named HRMT-23, was carried out with a special setup (Figure 5) that allowed testing three different full-scale collimator jaws [17]. In particular, a standard LHC collimator jaw in CFC and two HL-LHC collimator jaws in MoGr and CuCD. The former was made of a monolithic absorber block, 1 m long. The latter ones, instead, were made of eight blocks, 125 mm long each, in case of MoGr and 10 blocks, 100 mm long each, in case of CuCD. The experiment had a double purpose: to test the new collimator design and absorbers [18], as well as to gather significant information on the thermomechanical response of the recently developed materials, in order to benchmark the constitutive models implemented in the numerical simulations.

A stainless steel tank contained the three jaws vertically stacked, maintaining them under vacuum ($p \leq .001$ mbar). The tank was provided with three radiation-hard optical windows, which allow visual inspection of the jaws. A movable table connected to the jaw assembly ensured a horizontal movement up to 35 mm, to allow impacting the target at different depths from the absorber free surface. Besides, vertically, a movement of the whole tank with a stroke of ±140 mm permitted to choose the jaw to be impacted. An extensive instrumentation system was used to record online signals and to collect the data for offline postprocessing analyses. The instrumentation included strain gauges, temperature and ultrasound probes, optical microphones, water pressure sensors, optical fibers, high-speed, and high-definition cameras, as well as a laser-Doppler vibrometer. The mass of the test bench resulted to be roughly 1600 kg, with dimensions $1.2 \times 0.4 \times 2.1\ \mathrm{m}^3$. A total of 150 impacts, piling up 1E15 protons, was performed on the three jaws at increasing beam intensity (higher stored energy), to simulate both nominal operation conditions and accidental design case scenarios. Progressively increasing the beam intensity allows assessing the onset of material damage.

Depending on the collimator family, the design scenarios, in terms of accidental particle beam impact, are different. In the case of primary and secondary collimators (MoGr), the scenario foresees a direct impact of a particle pulse with stored energy equivalent to roughly 4.6 MJ. For tertiary collimators (CuCD), the design case is less demanding, as a direct impact can physically occur only for pulses with maximum stored energy of about 0.26 MJ.

During the experiment, the CuCD jaw was tested with a total of 18 pulses at high intensity, all with a vertical offset within ±5 mm with respect to the center of the absorber. Most of the impacts were close to the surface, with a horizontal offset of $\eta_x = -0.18$ mm (according to the reference system reported in Figure 1). 10 of the 18 pulses had a stored energy even higher than the accidental case scenario specified for the design of tertiary collimators. The MoGr jaw, instead, was impacted by 15 high intensity shots, with a maximum vertical offset of $\eta_y = -6.5$ mm and three main horizontal offsets $\eta_x = -3.05$ mm, -1.83 and -0.30 mm. The sigma of the beam was kept constant at 0.61 mm and the intensity of the beam was progressively increased. In addition, three shots with a more focused beam, with a 0.35 mm

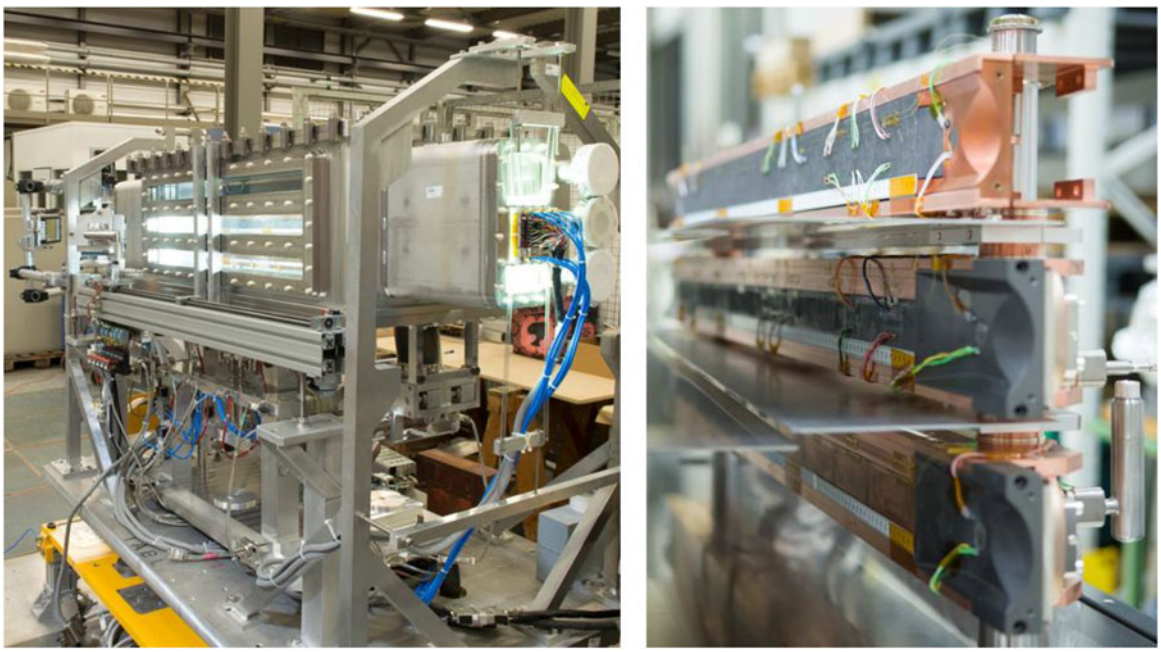

Figure 5. HRMT-23 experiment setup.

Table 4. Main shots recalled in the text for CuCD and MoGr. E_{tot} is the stored beam energy, σ is transverse size of the beam, η_x and η_y are the horizontal and vertical beam impact coordinates with respect to the reference system as defined in Figure 1

Impact identifier	E_{tot} (MJ)	σ (mm)	η_x (mm)	η_y (mm)
CuCD #1	0.21	0.35	−0.18	5.00
CuCD #2	0.20	0.35	−0.70	2.50
CuCD #3	0.43	0.35	−0.18	−5.00
CuCD #4	0.61	0.61	−3.05	−1.25
CuCD #5	1.22	0.61	−3.05	−1.25
MoGr #6	2.65	0.35	−1.75	0
MoGr #7	2.67	0.35	−1.05	0
MoGr #8	2.61	0.35	−0.18	0

sigma, were also performed at the highest intensity. The pulses were vertically centered, but with a decreasing depth, $\eta_x = -1.75$ mm, -1.05 mm and a grazing impact at -0.18 mm. The beam was focused in order to match and, in some case, exceed the HL-LHC energy density on the target, producing a comparable local response. Indeed, due to the experimental configuration of the HiRadMat facility, it is currently not possible to produce pulses with total stored energy equal to the design scenario foreseen for primary and secondary collimators. Notably, the maximum total energy achievable is about 60% of the 4.6 MJ involved in that scenario. The most relevant high-intensity shots for both materials are reported in Table 4, with the main beam parameters.

5. Postirradiation examination results

After the experiment, the tank was transferred to a storage area and then opened in the end of 2016, when the dose rate decreased down to few μSv/h. After a first visual inspection of the components, while the experiment was disassembled, in 2017 an extensive nondestructive test campaign was performed to assess the status of the collimator jaw components. The three absorbers material (CFC, MoGr, CuCD), downstream and upstream transitions, housing and cooling pipes were studied with different techniques. Herein, only the results concerning the new absorber materials, MoGr and CuCD, will be presented. Several measurements were carried out with the aim of investigating possible internal defects induced in the materials by the beam, not detectable from visual inspection, as well as quantifying visible damage. This is particularly important to benchmark the material constitutive model implemented in numerical simulations. Since the material used for collimator absorbers are advanced composites mostly created and developed *ad hoc* for this purpose, they are lacking literature data. The available ones allow the development of strength models independent of temperature and strain rate, which are on the contrary relationships necessary for the reproducibility of the physical conditions induced by the beam.

5.1. Postirradiation analysis for the CuCD blocks

In the CuCD jaw, as visible in Figure 6, signs of damage and plastic strain are quite evident especially on the copper cladding. Indeed, copper, having higher density than the bulk CuCD material (8.9 versus 5.4 g/cm^3), experiences higher energy absorption during the beam impact. For this reason, the pulses close to the free surface are certainly the most critical ones, inducing high energy densities in the copper layer.

Several pulses, at high intensity and different positions on the surface (η_y) and depth (η_x) of the absorbers, were performed with the purpose of evaluating different failure mechanisms. It is interesting to note that according to the depth of the impact, the damage induced into the material is different, as qualitatively introduced in Section 3.1. In particular, while low-depth shots or grazing pulses are responsible for spallation, microspallation, and microjetting, e.g. label *a* in Figure 6, high-depth impacts rather induce global plastic deformation and fractures on the free surface of the absorber, e.g. label *b* and *c* in Figure 6. Therefore, different nondestructive techniques were used to quantify both extensive damages, i.e. plastic deformation, and localized ones, i.e. grooves and scratches.

The plastic deformation induced on the free surface of the absorbers was quantified with a measurement of flatness of each block. The measurements were performed in the metrology lab at CERN with the optical machine ZEISS O-INSPECT 863. Figure 7 shows an example of the results obtained on the fifth block, the most damaged. As visible, the effect of the beam is quite evident on the middle part of block, between ±5 mm from the central axis, where all the pulses focused. This was observed for all the blocks, at least those presenting damages.

In Figure 8 (left), the flatness values measured for each block (red squares) are plotted as a function of the total absorber length, with 0 mm corresponding to the upstream of the first block and 1000 mm to the downstream of the tenth block. The flatness variation progressively increases moving from the upstream to the downstream region of the collimator, reaching a maximum in correspondence of half the length and then decreasing again. The maximum variation of flatness measured on the fifth block is around 1 mm, which is significant considering the tolerance of 100 μm, requested per specification for the LHC collimator absorbers. However, it has to be noted that the flatness change of CuCD is the result of 18 high intensity consequent impacts, including some pulses with intensity even higher than those occurring in the LHC and used as design scenarios. Images taken online immediately after the nominal accidental scenario for CuCD collimators showed a rather intact structure. This confirms that most of the damage took place in the successive higher intensity shots, performed to explore the damage threshold of the collimator material. This is defined as the maximum equivalent energy producing a damage recoverable through the 5th axis.

In the same plot, the energy density and total energy per longitudinal section estimated by energy deposition code is reported for comparison. The simulated pulse features a total energy of 1.22 MJ, sigma equal to 0.61 mm and an offset $\eta_x = -3.05$ mm (shot #5 in Table 4). As visible, the trend of the damage experienced by the absorbers over the length is quite well in agreement with the one of the total energy

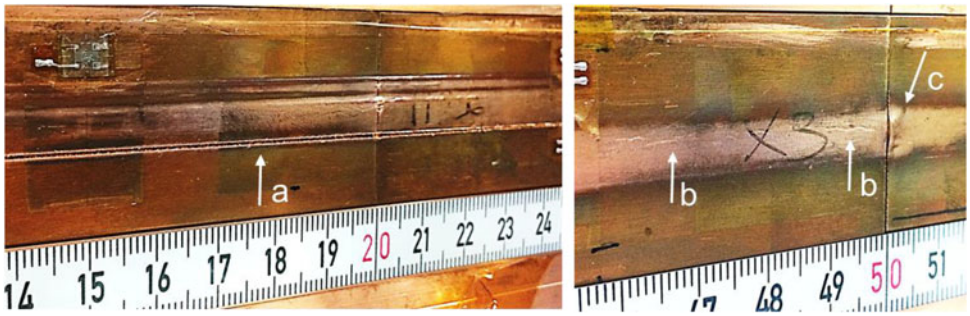

Figure 6. Examples of different damages on the free surfaces of the absorbers: grooves (a), small cracks (b) and plastic deformation (c).

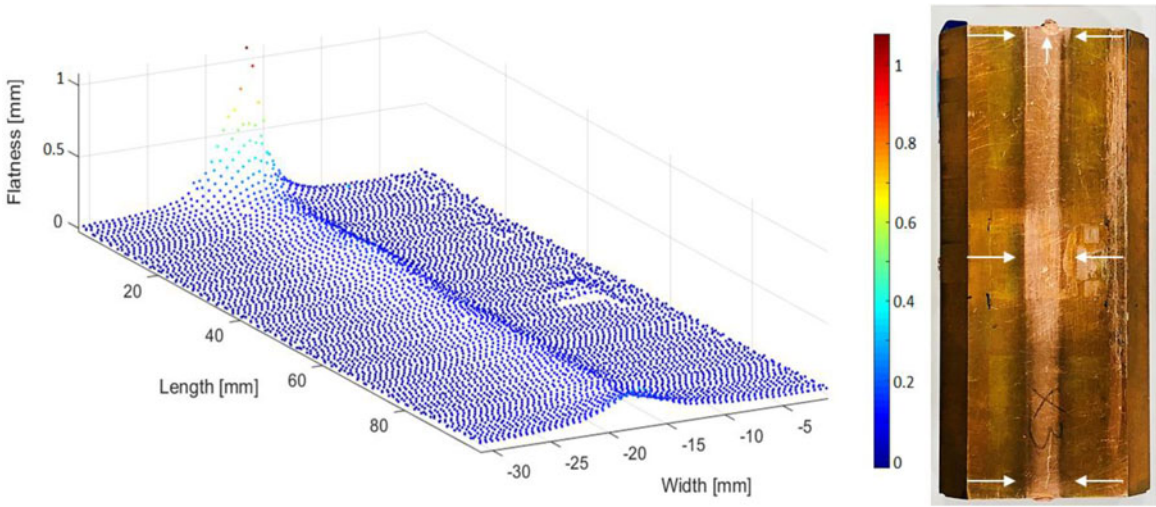

Figure 7. Flatness measurement on CuCD block 5 (left), picture of the block (right). The white arrows highlight the trace of the beam.

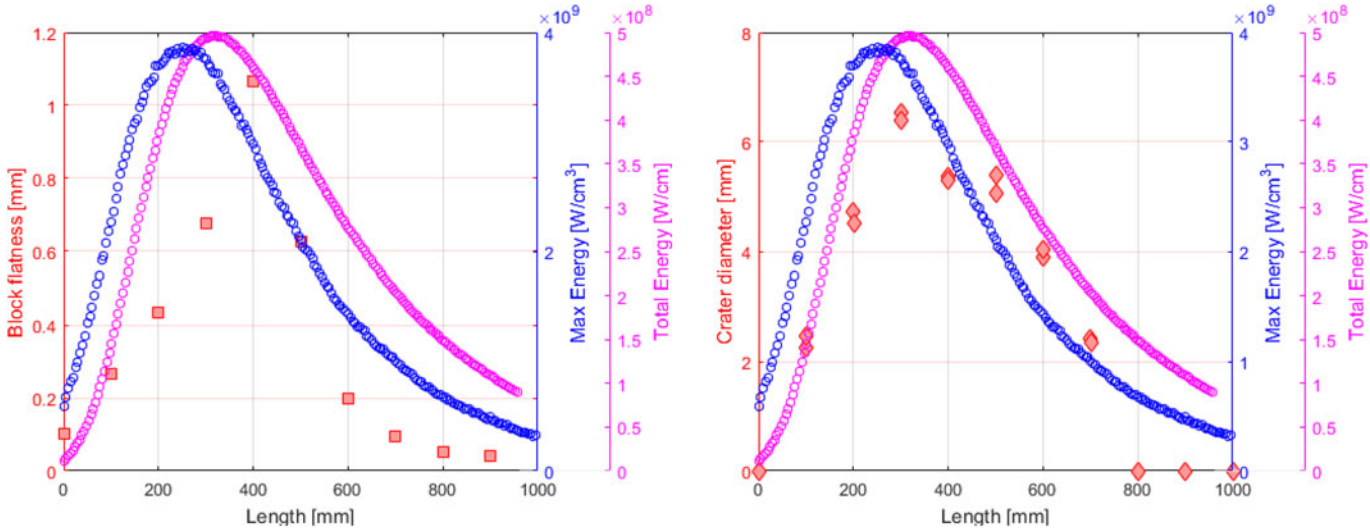

Figure 8. Results of the metrology measurements carried out on the 10 CuCD blocks. Flatness variation (left) and diameter values of the craters on the lateral surface (right). The energy and energy density (courtesy of E. Skordis) of shot #5 in Table 4, are reported in both plots for comparison.

deposition. This is reasonable, since the plastic deformation is a widespread damage rather than localized and therefore lies with the total energy stored in the material, instead of the energy density. However, it is important to point out that the change in flatness is most likely a cumulative damage induced by several impacts at high intensity and not only the specific impact considered for this comparison. Therefore, the maximum value of the total energy do not coincide perfectly with the maximum measured flatness variation.

Although the cumulative damage induced during the experiment in the CuCD jaw is significant as seen in Figure 7, the functioning of the collimator could be guaranteed thanks to the 5th axis. By moving vertically the jaw of ±10 mm from the damaged area, it would be possible to expose to the beam a fresh surface of the absorber with

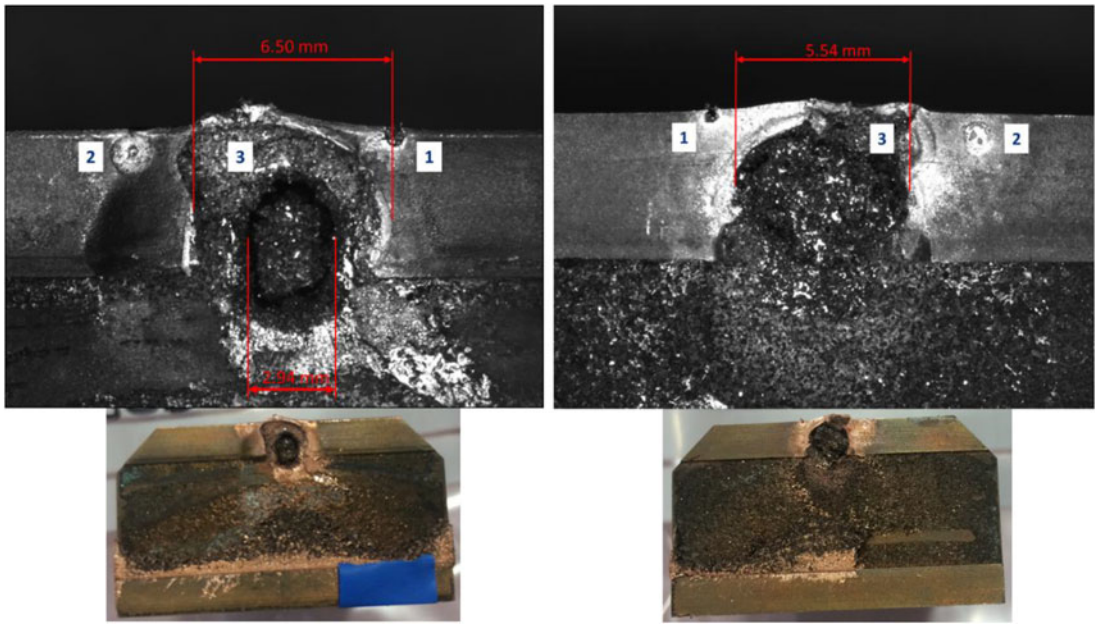

Figure 9. Lateral surfaces of CuCD block 4: upstream (left) and downstream (right). With reference to Table 4: crater 1, pulse #3; crater 2, pulse #2; crater 3, pulses #4 and #5.

lower flatness variation. Indeed, for the CuCD jaw, the damage threshold resulted to be about 1.22 MJ for a beam with $\sigma = 0.61$ mm.

Other interesting measurements were carried out to quantify dimension and position of the localized damages both on the free surface of each block and on the lateral faces. With the same optical machine used for the flatness measurements, ZEISS O-INSPECT 863, diameter and position of the craters appearing on the lateral surfaces of the blocks were estimated. Figure 9 reports the measurements performed on the fourth block, as an example.

As visible from the lateral surfaces of the fourth block, one can see two small damaged areas created by the pulses close to the surface (shots #2 and #3 in Table 4) and the predominant one, cumulative consequence of two impacts with the highest intensity at a depth of −3.05 mm from the surface (shots #4 and #5). The damages on the lateral surfaces of the blocks are substantial, but not unexpected. Indeed, microjetting and microspallation from the lateral surfaces of the blocks were recorded already online during the experiment with the high-speed camera.

The size of the predominant crater measured in correspondence of the upstream and downstream faces of each block is reported in the right plot of Figure 8 (red diamonds). The data are compared with the total energy and energy density for one of the two shots that induce the damage, the highest in terms of beam stored energy, 1.22 MJ (shot #5 in Table 4, energy five times higher than damage threshold). Although this is a quite localized damage, the trend of the crater dimensions over the total length of the absorbers is in good agreement with the one of the total energy deposition of the impact. Indeed, with such high intensity shot, the induced damage is wide. This means that the spall strength of the material is exceeded in a large volume and therefore the total amount of energy deposited into the absorber plays a key role with respect to the peak of the energy density.

3D topography measurements were performed on the free surface of the blocks with VEECO-NT3300 to quantify grooves and scratches. Three regions were selected for the measurements, upstream, middle and downstream part of the blocks. For each region, a portion of material with dimensions $1.2 \times 10/13$ mm, centered on the longitudinal axis of the block, was considered. Figure 10 shows an example of the upstream and downstream profiles scanned on the second block. One can clearly observe the two scratches at $\eta_y = \pm 5$ mm from the center, results of two pulses at depth $\eta_x = -0.18$ mm. In addition, the downstream profile shows the plastic deformation induced into the copper cladding in the center of the block.

The values of the maximum depth of the groove at $\eta_y = -5$ mm (impact #3 Table 4), measured on the first four absorbers (after the damage vanishes) are plotted in Figure 11, together with the energy and energy density. Since the impact is close to the surface (depth $\eta_x = -0.18$ mm), in this case the energy values are referred to the copper layer which covers the block, simulated together with the bulk CuCD core. Copper has higher density than CuCD and higher stopping power, as well. Therefore, as visible in the plot, the peak of the energy density moves towards the upstream region of the absorber full length. In particular, for the current case the maximum value appears on the second block, about 100 mm upstream of the case shown in Figure 8.

It is interesting to note that the trend of the damage over the length of the absorbers follows the energy density profile, as expected in case of localized damage as the considered one. In fact, this type of damage is produced by energy densities leading to stresses locally exceeding the material strength.

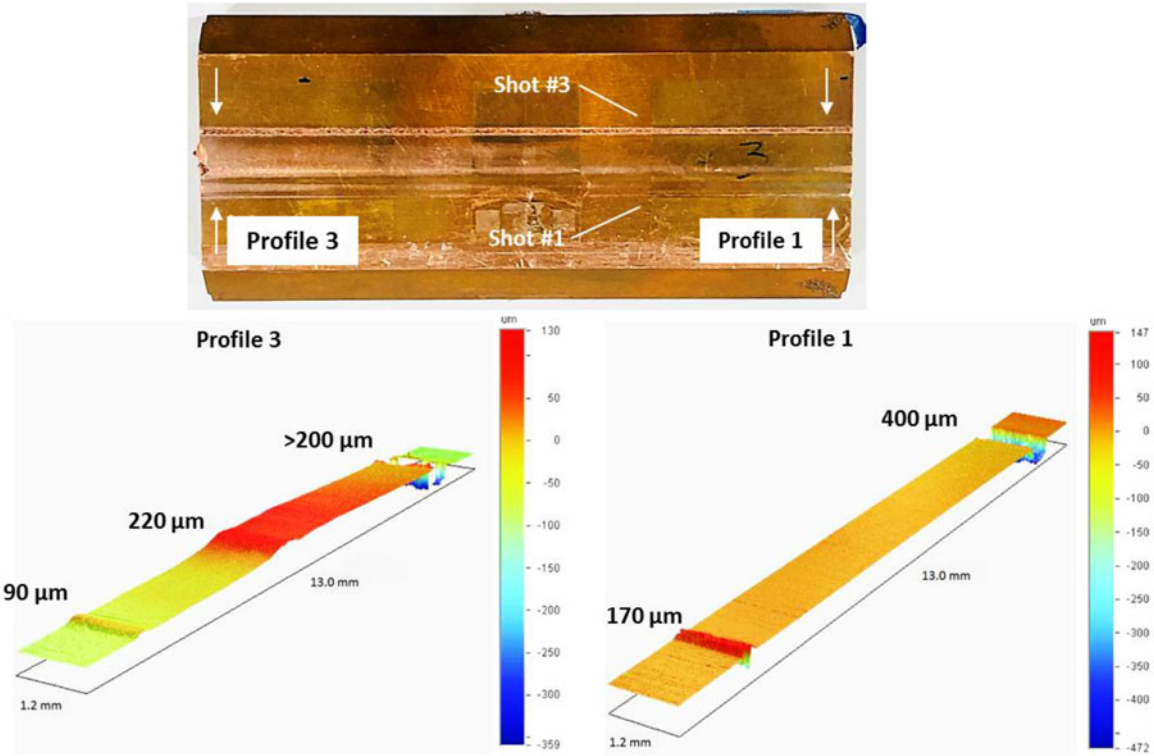

Figure 10. 3D topography measurements on CuCD block 2, upstream (profile 1) and downstream (profile 3) regions. Unit of measurement, µm.

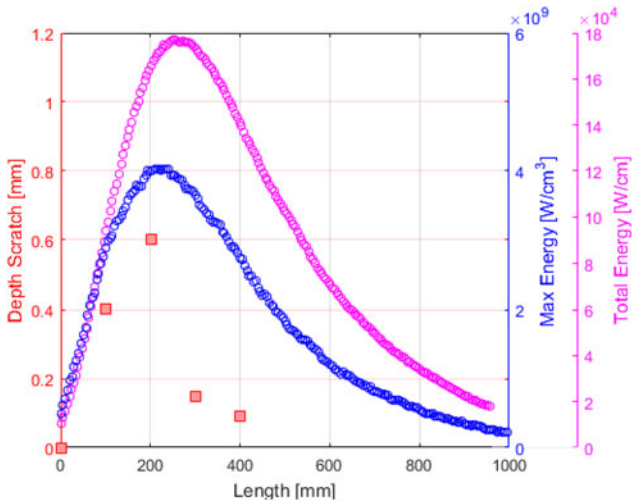

Figure 11. 3D topography results for the scratch at $\eta_y = -5$ mm on CuCD blocks. The absolute value of the depth is plotted, together with the total energy and the energy density (courtesy of E. Skordis) for shot#3 in Table 4.

5.2. Postirradiation analysis for the MoGr blocks

From the *post mortem* visual inspection, the MoGr blocks appeared considerably less damaged than the CuCD ones. Traces of the effect of the beam were limited to superficial deformation and/or local color change on the free surface of the absorbers. Moreover, on the lateral surfaces of the blocks no damage was detected for any beam impact conditions. This is an excellent result in view of the deployment of the MoGr choice as the HL-LHC baseline.

Although the effects of the beam impacts were almost imperceptible, nondestructive tests were carried out to try to quantify them and to detect potential internal damages. Therefore, for MoGr blocks, measurements of flatness, 3D topography and computed tomography (CT) were performed. The latter test was carried out only on MoGr blocks, since the higher density of CuCD limits the penetration of X-rays in samples with dimensions as the collimator block.

After the experiment disassembling, four MoGr absorbers were selected as the most interesting ones for the measurements: the first three blocks, showing the highest energy density, and the last one, which was loaded with the highest total energy (Figure 13). The remaining four blocks were coated with molybdenum and copper layers, and re-used for another HiRadMat test, not in the scope of this article.

Figure 12 shows the results of the flatness measurements performed on the second block, the most loaded in terms of energy density. A picture of the block is reported for comparison, to show the defect investigated with metrology measurements.

As visible, the free surface is considerably less damaged with respect to the case of CuCD blocks. The values of the flatness variation are in the order of µm, with respect to the mm-order-of-magnitude of the CuCD case. The effect of the beam is visible only in the center of the absorber, corresponding to the position where the material was impacted with the three highest intensity shots at low depths and with a focused beam (shots #6, #7, and #8 in Table 4). This is consistent with the fact that the most severe impact scenarios are those close to the free surface, as the stress wave generated by the thermal load is immediately reflected into tensile wave, with possible local spallation and pseudo-plastic deformation. Far from the free surface, the amplitude of the tensile wave quickly decreases because of the cylindrical

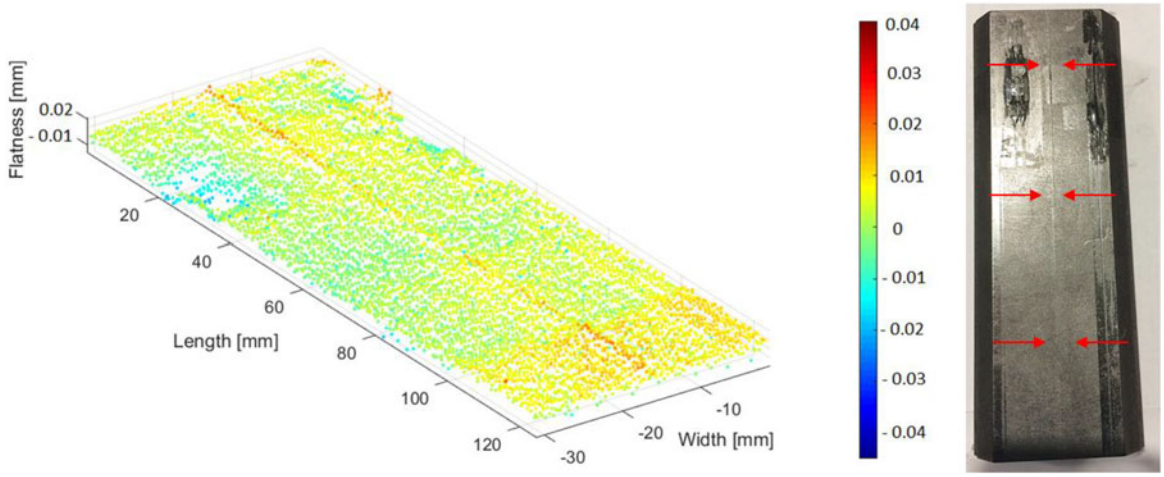

Figure 12. Flatness measurement on MoGr block 2 (left), picture of the block (right). The red arrows highlight the trace of the beam, the dark gray parts are remains of the glue used for the instrumentation.

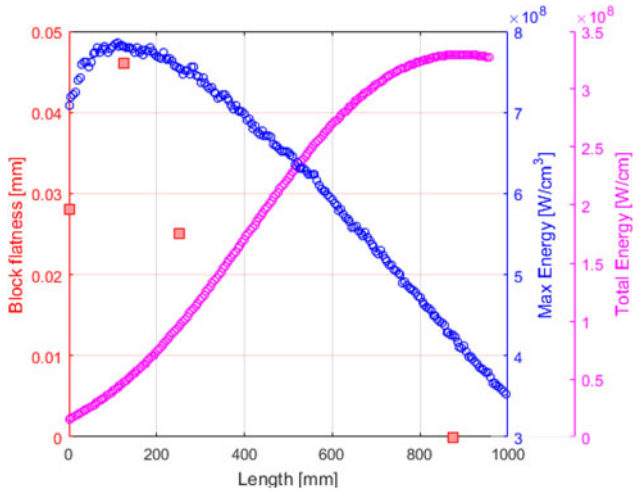

Figure 13. Results of flatness measurements on MoGr blocks. The data are plotted with the energy and energy density (courtesy of E. Skordis) for shot #6 in Table 4.

decay and internal friction, such that the amplitude of the tensile wave once generated on the surface of the material is less intense.

Similarly to the CuCD case, the values of the block flatness are plotted as a function of the total length of the active part of the jaw, together with the energy and the energy density (Figure 13). The simulated pulse is the number 6 in Table 4 (centered with an offset of $\eta_x = -1.75$ mm, sigma equal to 0.35 mm and a total energy of 2.65 MJ). Although the flatness measurements are more representative in case of an extensive damage, the trend of the values, despite the few points available, follows the longitudinal profile of deposited energy, as expected, since the damage is localized. Concerning this point, it is necessary to highlight that the peak value of the energy density reached for MoGr is lower than for CuCD (8E8 versus 4E9 W/cm^3), consistent with the different density of the material, in spite of the highest pulse intensity. Moreover, MoGr has lower coefficient of thermal expansion and higher melting temperature compared to CuCD. As a consequence, also the damages induced in the two materials are different, with MoGr being able to absorb a higher number of protons without significant damage, as requested for its use in primary and secondary collimators.

The 3D topography measurements provide quantitative information of localized defects with high precision. Figure 14 shows the results of the measurements carried out on the second block, the most loaded in the terms of energy density. It is interesting to note that the beam impact does not produce a scratch (negative values), as a height of 12–13 µm (positive values) was measured on the surface. This means that no spallation took place, implying that the stress generated was below the spall strength. However, the energy level was enough to induce a pseudo-plastic expansion in the material.

Since the effect of the beam on the surface seemed to be minor already from the preliminary visual inspection, roughness measurements were carried out, on a portion of material with dimension 7×7 mm far from the impacted region, for comparison. The surface roughness (R_a) of the MoGr is about 1.5 µm for the second block. This value is not negligible if compared to the height of the defect induced by the beam and therefore, it can be considered as the mean error of the measurements. As a result, one can conclude that after 15 high intensity impacts, the most loaded MoGr absorber reported a superficial defect of 12.5 µm ± 12%. This is a positive result, considering the 100 µm of flatness required per specification in operational conditions.

The surface traces were too small to be detected by computed tomography with ZEISS METROTOM equipment, for which a resolution of 26 µm was adopted while scanning the full block. However the images allow important observations concerning the structure of the bulk. From Figure 15, it is possible to observe some agglomerate of molybdenum carbides, most of them with ellipsoid shape and dimensions in the order of few mm. Carbide agglomerates were observed in other pristine samples of the same grade and in the most recently developed ones, as well. In the latter, however, the agglomerates present a spheroidal shape with a consequent lower anisotropy of the material. Moreover, some small

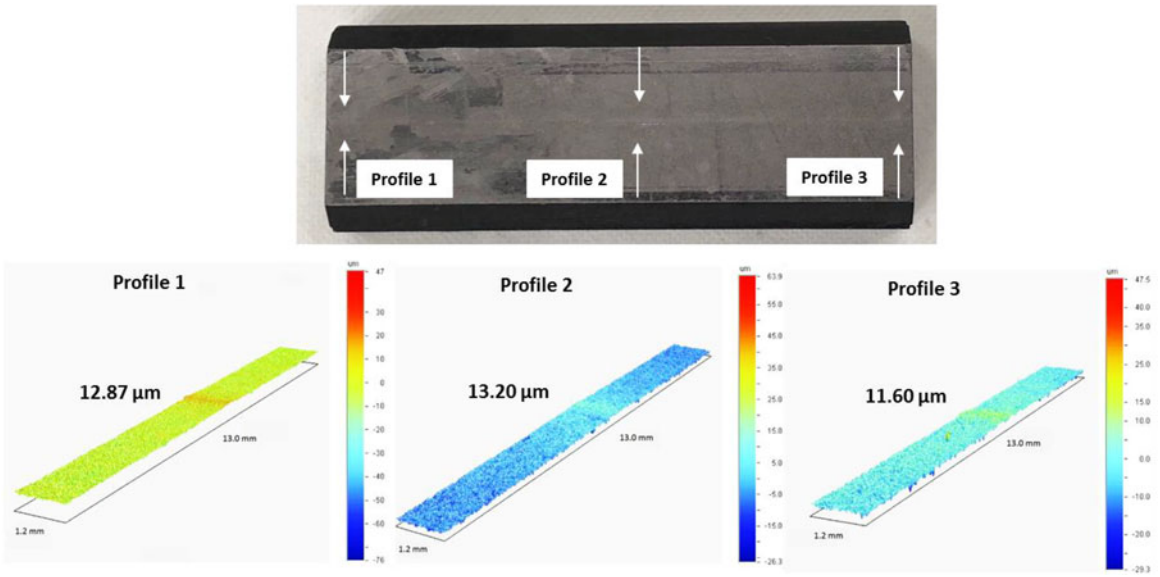

Figure 14. 3D topography measurements on the second MoGr block, upstream (profile 1), middle (profile 2) and downstream (profile 3) regions. Unit of measurement, µm.

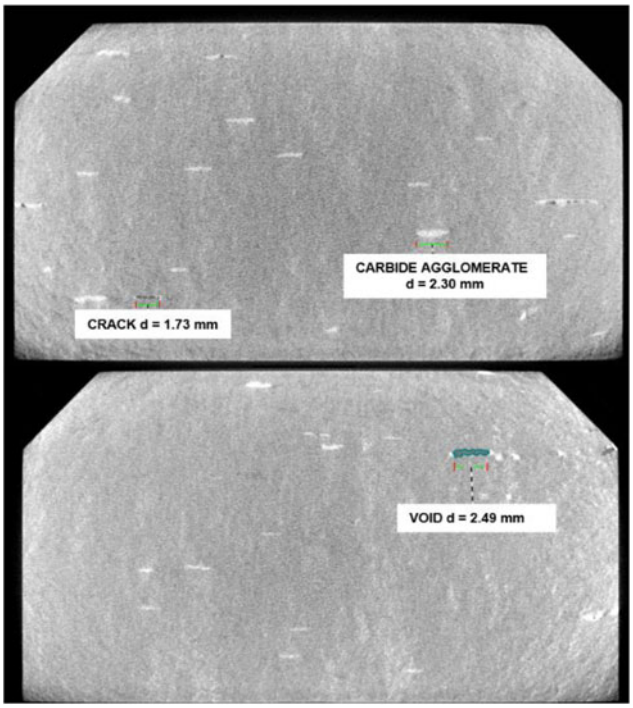

Figure 15. Computed tomography images, MoGr block 2 (above) and block 1 (below). Carbide agglomerates in white and cracks/voids in dark gray.

cracks or voids appear in correspondence of the carbide agglomerates. The most relevant (total volume of 2.84 mm^3) was found in the first block. However, their distribution is quite random in the bulk and not focused in the region close to the free surface of absorber, where the beam impacted. Therefore, these cracks can be unlikely attributed to a beam effect, but rather they are believed to be defects generated during the manufacturing process that, at the time of the experiment, was not optimized yet. Overall, the four blocks did not report any internal damage induced by the beam.

6. Conclusions

The results of an extensive nondestructive test campaign performed on two novel materials, Molybdenum–Carbide–Graphite and Copper–Diamond, proposed for the future HL-LHC collimators, were presented.

The materials were developed in the framework of an R&D activity that fostered collaboration between CERN and external companies. For a full validation, in addition to a thermophysical characterization of pristine samples, the materials were tested under high intensity beam impacts in the CERN HiRadMat facility. The aim was to assess the behavior of new composites under extreme conditions, covering design failures for LHC and HL-LHC. The beam impact test was successful and the materials survived to 15, in case of MoGr, and 18, in case of CuCD, high intensity shots reproducing the respective operative conditions and accidental case scenarios.

After irradiation, a *post mortem* examination was performed, including different nondestructive techniques, such as detailed visual inspections, metrology measurements, 3D topography, and computed tomography (CT). The measurement results were compared qualitatively with the simulated profiles of beam energy computed for each specific shot. From the results herein discussed, the following preliminary conclusions can be drawn.

The damage induced in the CuCD during the test was quite extensive, since the intensity reached in several pulses exceeded the one of the accidental design scenario. This material is considered a future upgrade of the LHC tertiary collimators made of Inermet®180. Significant damage was observed for beam intensity five times higher than the design scenario; based on previous beam impact experiments on Inermet®180 collimators [19], the increase in thermomechanical robustness guaranteed by CuCD is at least a factor of 14 (threshold of damage 1.22 MJ instead of 0.087 MJ).

Two different types of damage were identified, as a result of different impact depths. Low depth or grazing pulses

induced localized damages, i.e. scratches and grooves mainly localized on the most upstream blocks of the jaws, within about 300 mm from the impact location. In this case, the beam particles are absorbed mainly by the copper cladding, which has higher density than the core material, CuCD, and therefore reaches high energy density values in the upstream region. Indeed, the trend of the scratch-depth profile as a function of the distance from the impacting location is in good agreement with the longitudinal profile of the energy density deposition simulated on the copper cladding.

On the other hand, high-depth pulses induced plastic deformation on the free surface of the absorbers. This is attributed to the tensile waves generated on the free edges of the material after reflection of the compressive ones induced by the beam impact. The flatness variation reached values as large as 1 mm in the most loaded block. However, this is a cumulative effect of several high intensity beam shots. In a collimator, it would be possible to expose a flatter area to the beam by exploiting the 5th axis. Significant damages were induced on the lateral free surfaces of the absorbers, as well. Local melting was induced in the impacted region, creating craters with a maximum diameter of about 6 mm, in the most loaded block. In this case, the results reflected the trend of the total energy stored into the material during the shots rather than the one of the energy density.

The MoGr presented minor damage, even though the beam impacts were equivalent in terms of energy density to the accidental scenarios of primary and secondary collimators. In this case, it was not possible to determine a threshold of damage for the material since the energy density reached the maximum exploitable by HiRadMat facility. Traces of the beam effects were limited to superficial deformation, focused on the center of the blocks, where the three high-intensity shots were performed. 3D topography allows the estimation of the deformation that results in the order of 12.5 µm on the most loaded absorber. From computed tomography no internal damages induced by the beam were detected in the four blocks. The absorbers presented agglomerates of molybdenum carbides with an ellipsoidal shape, likely generated during the manufacturing process. In some case, cracks or voids originated from the agglomerates due to the high stress concentration at the ellipsoid sharp edges.

Acknowledgments

The authors would like to thank all the CERN colleagues who contribute to this project. M. Guinchard, O. Sacristan-de-Frutos, L. Bianchi for the thermophysical characterization of the materials; J. P. Rigaud, D. Glaude and A. Cherif for the metrology measurements; M. D. Jedrychowski and G. A. Izquierdo for the computed tomography measurements. The authors would like to thank also E. Skordis for providing the FLUKA energy density maps.

Disclosure statement

No potential conflict of interest was reported by the authors.

Funding

The research leading to these results has received funding from the European Commission under the FP7 Research Infrastructures project EuCARD-2, grant agreement No 312453. This project has received funding from the European Union's Horizon 2020 Research and Innovation program under Grant Agreement No 730871.

ORCID

Giorgia Gobbi http://orcid.org/0000-0001-7127-1287

References

[1] O. Brüning, P. Collier, P. Lebrun, S. Myers, R. Ostojic, J. Poole and P. Proudlock, LHC Design Report. CERN Yellow Reports: Monographs, Geneva, Switzerland, 2004.

[2] G. Apollinari, I Béjar Alonso, O. Brüning, P. Fessia, M. Lamont, L. Rossi and L. Tavian, High-Luminosity Large Hadron Collider (HL-LHC) Technical Design Report v.0.1. CERN Yellow Reports: Monographs 4, Geneva, Switzerland, 2017.

[3] R. Assmann, R. Aßmann, M. Brugger, L. Bruno, H. Burkhardt, G. Burtin, B. Dehning, C. Fischer, B. Goddard, E. Gschwendtner, M. Hayes, J. B. Jeanneret, R. Jung, V. Kain, M. Lamont, R. Schmidt, E. Vossenberg, E. Weisse, J. Wenninger, I. Baishev and D. Kaltchev, Requirements for the LHC collimation system, Proceedings of EPAC 2002, Paris, France, 2002.

[4] E. Quaranta, A. Bertarelli, N. Biancacci, R. Bruce, F. Carra, E. Métral, S. Redaelli, A. Rossi and B. Salvant, Towards optimum material choices for HL-LHC collimator upgrade, Proceedings of IPAC 2016, Busan, Korea, 2016.

[5] A. Bertarelli, G. Arnau Izquierdo, F. Carra, A. Dallocchio, M. Gil Costa and N. Mariani, Research and Development of Novel Advanced Materials for Next-Generation Collimators, IPAC 2011, San Sebastián, Spain, 2011.

[6] A. Bertarelli, F. Carra, N. Mariani and S. Bizzaro. Development and testing of novel advanced materials with very high thermal shock resistance, Proceedings of Tungsten, Refractory and Hardmetals Conference, OR, 2014.

[7] A. Bertarelli, F. Carra, M. Garlasche, P. Gradassi, J. Guardia Valenzuela, S. Sgobba and T. Tsarfati, Innovative MoC – graphite composite for thermal management and thermal shock applications, 2015 31st Thermal Measurement, Modeling & Management Symposium (SEMI-THERM), San José, 2015.

[8] I. Efthymiopoulos, C. Hessler, H. Gaillard, D. Grenier, M. Meddahi, P. Trilhe, A. Pardons, C. Theis, HiRadMat: a new irradiation facility for material testing at CERN, IPAC 2011, San Sebastián, Spain, 2011.

[9] J. Guardia-Valenzuela, A. Bertarelli, F. Carra, N. Mariani, S. Bizzaro and R. Arenal, Development and properties of high thermal conductivity molybdenum carbide - graphite composites, Carbon, vol. 135, pp. 72, 2018.

[10] M. Borg, A. Bertarelli, F. Carra, P. Gradassi, J. Guardia-Valenzuela, M. Guinchard, G. Arnau Izquierdo, P. Mollicone, O. Sacristan-de-Frustos and N. Sammut. Thermostructural characterization and structural elastic property optimization of novel high luminosity LHC collimation materials at CERN, Phys. Rev. Accel. Beams, vol. 21, no. 3, pp. 031001, 2018.

[11] N. Mariani. Development of Novel, Advanced Molybdenum-based Composites for High Energy Physics Applications, CERN Thesis-2014-363, 2014.

[12] F. Carra. Thermomechanical response of advanced materials under quasi-instantaneous heating, PhD Thesis, Politecnico di Torino, Italy, 2017.

[13] G. Battistoni, F. Cerutti, A. Fasso, A. Ferrari, S. Muraro, J. Ranft, S. Roesler, and P.R. Sala, The FLUKA code: description and benchmarking, AIP Conference Proceedings, 2007.

[14] S. Agostinelli, J. Allison, K. Amako, J. Apostolakis, H. Araujo, et al., GEANT4 – a simulation toolkit, Nuclear Instruments and Methods in Physics Research Section A: Accelerators, Spectrometers, Detectors and Associated Equipment, vol. 506, no. 3, pp. 250–303.

[15] Ansys Mechanical User's Guide – Release 15.0, ANSYS, Inc. 2013. Available from https://www.scribd.com/document/341072012/ANSYS-Mechanical-User-s-Guide-pdf

[16] Ansys AUTODYN User's Manual – Release 15.0, ANSYS, Inc. 2013. Available from https://www.sharcnet.ca/Software/Ansys/17.0/en-us/help/wb_adyn/autodyn_book.html

[17] A. Bertarelli, A. Dallocchio, M. Garlasche, L. Gentini, P. Gradassi, M. Guinchard, S. Redaelli, A. Rossi, *et al.*, 2014. Novel materials for collimators at LHC and its upgrades, Proceedings of HB2014, East Lansing, MI. ISBN 978-3-95450-173-1, pp. 438–442. Available from http://accelconf.web.cern.ch/AccelConf/HB2014/papers/tho4ab03.pdf

[18] F. Carra, A. Bertarelli, A. Dallocchio, L. Gentini, P. Gradassi, G. Maitrejean, A. Manousos, N. Mariani, N. Mounet, E. Quaranta, S. Redaelli, V. Vlachoudis, Mechanical engineering and design of novel collimators for HL-LHC, Proceedings of IPAC 2014, Dresden, Germany, 2014. ISBN:978-3-95450-132-8, pp. 369–372. doi:10.18429/JACoW-IPAC2014-MOPRO116

[19] M. Cauchi, O. Aberle, R.W. Assmann, A. Bertarelli, F. Carra, K. Cornelis, A. Dallocchio, D. Deboy, L. Lari, S. Redaelli, *et al.*, High energy beam impact tests on a LHC tertiary collimator at the CERN high-radiation to materials facility, Phys. Rev. ST Accel. Beams, vol. 17, no. 2, pp. 021004, 2014. ISBN 978-3-95450-173-1 pp. 438–442. Available from http://accelconf.web.cern.ch/AccelConf/HB2014/papers/tho4ab03.pdf